Local negative permittivity and topological-phase transition in polar skyrmions

S. Das[1,2*], Z. Hong[3,4*], V.A. Stoica[3*], M. A. P. Gonçalves [5,6,7*], Y.T. Shao[8], E. Parsonnet[2], E. J. Marksz[9], S. Saremi[1], M. R. McCarter[2], A. Reynoso[2], C. J. Long[9], A. M. Hagerstrom[9], D. Meyers[1], V. Ravi[1], B. Prasad,[1] H. Zhou[10], Z. Zhang[10], H. Wen[10], F. Gómez-Ortiz[6], P. García-Fernández[6], J. Bokor[11], J. Íñiguez[5,7], J.W. Freeland[10], N. D. Orloff[9], J. Junquera[6], L.Q. Chen[3], S. Salahuddin[11], D. A. Muller[8,12], L.W. Martin[1,13], R. Ramesh[1,2,13]

[1] Department of Materials Science and Engineering, University of California, Berkeley, California 94720, USA

[2] Department of Physics, University of California, Berkeley, California 94720, USA

[3] Department of Materials Science and Engineering, The Pennsylvania State University, University Park, Pennsylvania 16802, USA

[4] Department of Mechanical Engineering, Carnegie Mellon University, Pittsburgh, PA 15213, USA.

[5] Materials Research and Technology Department, Luxembourg Institute of Science and Technology (LIST), 5 avenue des Hauts-Fourneaux, L-4362 Esch/Alzette, Luxemburg

[6] Departamento de Ciencias de la Tierra y Física de la Materia Condensada, Universidad de Cantabria, Cantabria Campus Internacional, Avenidad de los Castros s/n, E-39005 Santander, Spain

[7] Physics and Materials Science Research Unit, University of Luxembourg, 41 Rue du Brill, L-4422 Belvaux, Luxembourg

[8] School of Applied and Engineering Physics, Cornell University, Ithaca, NY, USA

[9] National Institute of Standards and Technology, Boulder, CO, USA

[10] Advanced Photon Source, Argonne National Laboratory, Argonne, IL, USA

[11] Department of Electrical Engineering and Computer Sciences, University of California, Berkeley, CA, USA

[12] Kavli Institute at Cornell for Nanoscale Science, Ithaca, New York 14853, USA

[13] Materials Sciences Division, Lawrence Berkeley National Laboratory, Berkeley, California 94720, USA

(* these authors contributed equally)

(Email: sujitdas@berkeley.edu , rramesh@berkeley.edu)

Topological solitons such as magnetic skyrmions have drawn enormous attention as stable quasi-particle-like objects. The recent discovery of polar vortices and skyrmions in ferroelectric-oxide superlattices, exhibiting exotic physical phenomena, has opened up new vistas to explore topology, emergent phenomena, and approaches for manipulating such features with electric fields.[1,2] Using macroscopic dielectric measurements, coupled with direct scanning convergent-beam electron diffraction (SCBED) imaging of the local polarization and electric-field profiles at the atomic scale, theoretical phase-field simulations, and second-principles calculations, we demonstrate that polar skyrmions in $(PbTiO_3)_n/(SrTiO_3)_n$ superlattices are distinguished by a sheath of negative permittivity at the periphery of each skyrmion. This enables a strong enhancement of the effective dielectric permittivity as compared to individual $SrTiO_3$ and $PbTiO_3$ layers. Moreover, the response of these topologically protected structures to electric field and temperature reveal a reversible phase transition from a topologically protected skyrmion state (with a topological charge of +1) to a trivial uniform ferroelectric state (topological charge of 0), accompanied by a large tunability of the dielectric permittivity. Pulsed-switching measurements show a time-dependent evolution and recovery of the skyrmion state (and the macroscopic dielectric response). The interrelationship between the topological and the dielectric properties presents a unique opportunity to simultaneously manipulate both of them by a single, and easily controlled, stimulus, the applied electric field.

Spatially complex, real-space topological configurations and their phase transitions have recently emerged as a fertile playground in condensed-matter physics.[3, 4] Although the focus has been on spin textures in magnets,[4,5,6] leading to the formation of skyrmions and related topologically protected states, in recent years there has been renewed efforts to discover analogous charge textures in, for example, ferroelectrics.[7-10] With the discovery of such polar textures (*e.g.*, vortices and skyrmions), it is of both fundamental and practical interest to understand the microscopic and macroscopic nature of their dielectric response and the possibility of a field-driven topological-phase transition.[1,2]

In parallel, the possibility of capturing "negative permittivity" states in ferroelectrics, either in the temporal (*i.e.*, dynamical) or spatial (*i.e.*, in equilibrium) domain has drawn the attention of scientists and engineers alike.[11,12,13,14,15,16,17,18,19] The concept of negative capacitance was developed in monodomain ferroelectric capacitors by considering that upon transitioning to a ferroelectric state, a material develops a classic "double-well potential energy" landscape. The minima of these wells represent the equilibrium state of the material and the curvature of the energy landscape dictates that small electric-field perturbations should give rise to classical positive capacitive response (*i.e.*, positive permittivity). It was proposed, however, that if one could place the material in the region between these two states (*i.e.*, in a region of negative curvature of the energy landscape) it could give rise to a negative-capacitive response (*i.e.*, negative permittivity) under electric-field excitation.[2,20] In a capacitor heterostructure comprised of an ideal ferroelectric capacitor (capacitance C_F) in series with a regular dielectric capacitor (capacitance C_D), the overall capacitance $C = (C_F^{-1} + C_D^{-1})^{-1}$ has to be positive for thermodynamic stability. But if $C_F < 0$, the total C will be larger than any of the two constituent capacitors taken independently. Accessing this regime, however, remains a challenge in the static sense[14,16,18]: if the capacitor is driven by a

voltage the region of negative curvature is unstable. Researchers have explored approaches wherein the capacitor is driven by a charge, that can be simply controlled in an electrostatically coupled ferroelectric/dielectric series capacitor.[13] If the dielectric is a dielectrically stiff material, it will effectively suppress the spontaneous polarization of the ferroelectric, thus stabilizing the paraelectric state even above the transition temperature.[18] The negative-capacitance effect was first observed in metal-semiconductor interfaces.[21] Transient negative capacitance behavior of epitaxial ferroelectric $PbZr_{0.2}Ti_{0.8}O_3$ films, $PbZr_{0.2}Ti_{0.8}O_3/SrTiO_3$ heterostructures, $BaTiO_3/SrTiO_3$ bilayers, and $Al_2O_3/BaTiO_3$ bilayers have been investigated through the dynamic switching behavior governed by classical domain nucleation and growth.[15, 22] Recent work has further demonstrated that in multidomain ferroelectric emergent polar structures – as in the vortices found in $(PbTiO_3)_n/(SrTiO_3)_n$ superlattices – the complex polar order, while producing an overall positive dielectric permittivity, exhibits regions of varying dielectric susceptibility including areas of local negative-capacitive response in the $PbTiO_3$ layers.[2]

The recent discovery of chiral polar skyrmions in $(PbTiO_3)_n/(SrTiO_3)_n$ superlattices by the interplay of elastic, electrostatic, and gradient energies with a topological number of +1 raises a fundamentally important question: do such skyrmions also exhibit a spatial distribution of varying dielectric susceptibility?[1] Here, we demonstrate a strong enhancement of the out-of-plane dielectric permittivity and that this is a direct consequence of a negative-permittivity region that forms at the periphery of each skyrmion. In this region, the polarization is more susceptible to external stimuli than the inner core or the outer regions of the skyrmions. This is further confirmed by second-principles calculations, phase-field modeling, and direct microscopic measurements of the local potential energy via scanning convergent-beam electron diffraction (SCBED) experiments using an electron microscopy pixel array detector (EMPAD). The macroscopic

permittivity also exhibits a large electric-field tunable response which arises from the conversion of the skyrmions into a uniformly polarized state (topological-phase transition), as evidenced by both electric-field- and temperature-dependent dielectric measurements and synchrotron-based-diffraction studies, which are supported by second- principles calculations and phase-field simulations.

A series of $[(PbTiO_3)_{16}/(SrTiO_3)_{16}]_m$ superlattices (m = 3, 5, 8) and $(SrTiO_3)_{16}/(PbTiO_3)_{16}/(SrTiO_3)_{16}$ trilayers (where the subscript numbers refer to the number of unit cells) as well as 50 nm-thick $SrTiO_3$ and 50 nm-thick $PbTiO_3$ single-layer thin films all grown on TiO_2-terminated single-crystalline $SrTiO_3$ (001) substrates, with epitaxial $SrRuO_3$ top and bottom electrodes (all films produced via reflection high-energy electron diffraction (RHEED)-assisted pulsed-laser deposition; Methods) were synthesized for this study.[1] Plan-view scanning transmission electron microscopy (STEM) images of the superlattices reveal an array of skyrmion bubbles (8-9 nm in diameter) (Supplementary Fig. 1a), the formation of which has been confirmed by second-principles calculations (Supplementary Fig. 1b)[1] which reveal that they are indeed electric analogs of magnetic skyrmions and have a mathematically definable and characteristic skyrmion number of +1 (Supplementary Table 1). Three-dimensional reciprocal space mapping (RSM) studies of the superlattices about the 002-diffraction condition show satellite peaks around the film peak along the in-plane directions (side lobes), corresponding to an ordered phase (*i.e.*, the skyrmion phase) with a periodicity of 8-9 nm (Supplementary Fig. 2).[1] In all heterostructures studied – the superlattices, trilayers, and single-layer films – all layers were found to be coherently strained to the underlying $SrTiO_3$ substrate, confirming that the strain state in all cases is the same. Macroscopic measurements of the dielectric permittivity (extracted from the experimentally measured capacitance, Figure 1a) and dielectric loss (Supplementary Fig. 3) as a function of

electric field (applied normal to the surface) for $[(PbTiO_3)_{16}/(SrTiO_3)_{16}]_m$ superlattices (m = 3, 5, 8) and $(SrTiO_3)_{16}/(PbTiO_3)_{16}/(SrTiO_3)_{16}$ trilayers were completed. The superlattices and the trilayer exhibit a strong enhancement of zero-field dielectric permittivity compared to the various single-layer $SrTiO_3$ and $PbTiO_3$ heterostructures (Fig. 1a), contrary to what is expected to be a decrease in the overall permittivity as calculated using a conventional "dielectrics in series" scenario ("Series permittivity" dotted line, Fig. 1a and Supplementary Fig. 4). These structures also show large electric-field tunability (~70-80% for the various superlattices and trilayers under 1500 kV/cm fields); which is significantly different from that of the single-layer $SrTiO_3$ (~7% under 700 kV/cm) and $PbTiO_3$ (~2% under 700 kV/cm) (Fig. 1a) as well as the polar vortices [which form when the superlattice is synthesized on $DyScO_3$ (110)], which show the electric field tunability of almost 45% (Supplementary Fig. 4, Supplementary Table 2).[2]

In order to understand the microscopic origins of the dielectric observations, we carried out detailed phase-field simulations and second-principles calculations for $[(PbTiO_3)_{16}/(SrTiO_3)_{16}]_8$ superlattices to extract measures of the dielectric permittivity (Methods and Supplementary Information and Supplementary Fig. 5). The normalized electric-field-dependent permittivity from both these theoretical approaches are captured [red dashed (phase-field) and green dashed (second-principles) lines, Fig. 1b] and closely follow the experimental data. The origin of such an enhancement in the dielectric permittivity can be unraveled from the theoretical simulations which provide spatially-resolved maps of the local permittivity (Fig. 2). Taking a real-space representation of the skyrmions (left, Fig. 2a), we can extract the corresponding spatial distribution of the dielectric permittivity within the $PbTiO_3$ layer from the phase-field simulations (right, Fig. 2a). This indicates an unusual dielectric state within the $PbTiO_3$ layer wherein there are regions of negative permittivity (blue/cyan regions, Fig. 2a and

Supplementary Fig. 6) at the surface of the skyrmion. Inside and outside this surface region, the permittivity is positive (yellow regions, Fig. 2a). The inverse of the dielectric permittivity from the second-principles calculations for a single skyrmion (Fig. 2b and Supplementary Fig. 7) also reveals the existence of a region of negative permittivity at the periphery of the skyrmions. The corresponding electric susceptibility (Fig. 2c and Supplementary Fig. 7) also reveals that the surface of the skyrmion exhibits the highest electric susceptibility and deforms with an applied electric field to increase/decrease the volume of the core.

Based on these calculations, it is possible to reconstruct the macroscopic dielectric permittivity of the $[(PbTiO_3)_{16}/(SrTiO_3)_{16}]_8$ superlattices (Methods and schematically illustrated in Fig. 2d). While the superlattices consist of $SrTiO_3$ and $PbTiO_3$ layers connected in series, the $PbTiO_3$ layers have two regions, one inside/outside the skyrmions with positive permittivity and the other at the surface of the skyrmions with negative permittivity, which are electrically parallel to each other (Fig. 2d). Based on this structure, an "effective circuit" model for this stack (right, Fig. 2d) enables us to calculate the net permittivity of the superlattice as a function of the individual dielectric permittivities of the $SrTiO_3$ (ε_1), $PbTiO_3$ within/without the skyrmion (ε_2), and $PbTiO_3$ within the skyrmion boundary (ε_3) (Fig. 2e-f). There are a few key conclusions that emerge from these calculations: First, there are no values of the individual dielectric permittivities ($\varepsilon_i, i = 1, 2, 3$) for which the effective permittivity of the superlattice is higher than that of the $SrTiO_3$ or $PbTiO_3$ layers by themselves, except when there are regions of negative permittivity (Fig. 2e-f). This includes allowing the values of individual layer permittivities to be considerably larger than their bulk values (*e.g.*, here we have explored values of the permittivity of $SrTiO_3$ (ε_1) from 0-500, for $PbTiO_3$ within/without the skrymion (ε_2) from 0-500, and $PbTiO_3$ within the skyrmion boundary (ε_3) to be as large as 1000). Said another way, it is not possible in either a simple series

model or in our adjusted equivalent circuit model to achieve the large permittivity values simply by increasing the permittivity of any individual component or combination of layer values. When negative permittivity is assigned to the skyrmion-boundary region, however, these calculations do reveal an enhancement of the effective dielectric permittivity (Fig. 2e). Based on these calculations and the experimental measurements (which are only weakly dependent on the frequency in this range; Fig. 1a, details of the frequency dependence of capacitance and permittivity are presented in Supplementary Figs. 8 and 9), we estimate the permittivity of the skyrmion surface to be ~ -500, which is qualitatively consistent with phase-field simulations and second-principles calculations (Fig. 2a-c). Comparisons of the dielectric permittivity of the vortex and the skyrmion (Supplementary Fig. 4) show that they are significantly different from each other. We note that although large enhancements in dielectric permittivity have been observed in other systems (relaxor ferroelectrics, functionally graded ferroelectrics, etc.) [19, 23], the fundamental physical origins of the enhancement in the dielectric response in this case is completely different from other possible phenomena (*e.g.*, Maxwell-Wagner effects, inductor-capacitor (LC) resonance)[24,25, 26], again suggesting that it is intimately associated with the skyrmion state (Supplementary Fig. 8).

The possibility of the existence of such a region of negative permittivity at the skyrmion surface and the potential-energy landscape across the skyrmion can be directly probed using scanning convergent beam electron diffraction (SCBED) experiments. These imaging experiments were carried out in cross-section samples so that we could image both the Neél and Bloch components edge-on (Fig. 3a).[1] The SCBED experiments were performed using an electron microscopy pixel array detector (EMPAD) (details in Methods and Supplementary Fig. 10) which records the full momentum distribution (*i.e.*, the electron diffraction pattern) at every scan position, providing information to measure both the ferroelectric polarization and electric field

simultaneously and independently (Fig. 3b-d). For this study, we focused on the deflection of the (000) beam since there are fewer polarity effects. The polarization direction is quantitatively determined from the diffraction intensity differences of Friedel pairs, such as the (100)/($\bar{1}$00) and (001)/(00$\bar{1}$) for the x and z component of polarity, respectively (Fig. 3b, Supplementary Fig. 10, and Methods).[2] The long-range electric fields can be reconstructed from the deflection of the entire CBED pattern due to the Lorentz force (Fig. 3c, Supplementary Fig. 10, and Methods).[2, 27] Focusing along the dashed horizontal line profile (Fig. 3b,c), which goes through the center of a skyrmion, we can extract information about both the Neél and Bloch components of the skyrmion (Fig. 3a)[1] by measuring the polarization (P_z) and electric field (E_z) along this line (Fig. 3d). The magnitude of the measured polarization was calibrated using the polarization of $PbTiO_3$ as reference.[28] With both the measured electric field and polarization, we can calculate the local potential energy of the system using $dG = EdP$ (Methods).[2] The estimated potential-energy (G) as a function of P_z across the skyrmion (Fig. 3e; details in Methods) reveals the existence of a local potential-energy maxima ($\partial^2 G/\partial P^2 < 0$) at the location of the skyrmion wall, where P_z is small (Fig. 3e). This provides direct microscopic evidence of regions having negative curvature of the free energy (*i.e.*, negative permittivity) in the skyrmion walls.

Having identified a possible source of the enhancement of overall permittivity associated with the negative permittivity at the skyrmion surface, we now discuss the changes in the dielectric response and the topological structure with electric field (Fig. 4). Both phase-field simulations and second-principles calculations reveal that when an electric field is applied along the out-of-plane direction (parallel/antiparallel to the uniform polarization of the skyrmion cores) it progressively expands (shrinks) for parallel (antiparallel) fields and ultimately the entire material becomes uniformly poled with increasing field (Fig. 4a-c and Supplementary Figs. 11, 12). To validate these

calculations, we performed electric-field-dependent X-ray diffraction RSM studies (Methods) to observe the skyrmion evolution[1] as a function of applied electric field. The electric-field-dependent RSM studies (Fig. 4d-e and Supplementary Fig. 13) show the systematic disappearance of the skyrmion-satellite peaks with increasing electric field, indicating field-induced structural changes related to the skyrmions (Fig. 4e, Supplementary Figs. 13b and 14). The external electric field in the out-of-plane direction breaks the symmetry and tends to align the dipoles along the direction of the external field in order to minimize the energy (details in Methods and Supplementary). Additional electric-field-dependent studies of first-order and second-order satellite peaks (Supplementary Figs. 14, 15) were used to reveal more insight about the evolution of the skyrmion size with electric field. While the intensity of the first-order satellite peaks decreases with electric field, the second-order satellite peaks (which are absent at zero applied field) are found to emerge under applied field. As a first approximation (ignoring the domain boundary width and its variation with electric field) changes in the skyrmion size should correspond to variations in the intensity of the measured satellites which can be described based on the Fourier transformation of up-and-down periodic nanodomain structure (Supplementary Fig. 14, 15)[29,30] that gives a relationship between the domain fraction and intensity of satellites as:

$$\frac{I(f)}{Imax} = \sin^2(\pi m f) \quad (1)$$

where *I(f)* is the measure intensity, I_{max} is the maximum intensity, *m* is the order of the scattering peaks (*m* = 1 is first order, *m* = 2 is second order, etc.), and *f* is the relative domain fraction (here replaced with the skyrmion fraction). Applying this formalism to our samples indicates that for *f* ≈ 0.5 the amplitude of the second-order satellites should vanish, while the first-order satellites should be at maximum amplitude; consistent with what is observed at zero-applied field. Under application of an electric field, the second-order satellites grow in intensity while the first-order

satellites decrease, indicating that not only the skyrmion fraction, but their size, has changed. The skyrmion fraction extracted from the experimental data is in good agreement with the simulated field-dependent skyrmion fractions (Supplementary Fig. 14d, 15). Thus, such an electric-field-driven change in the size of the skyrmion directly impacts the effective dielectric permittivity as well as the negative component of permittivity (Supplementary Fig. 14e, 16The calculated and the experimentally measured dielectric permittivity are in close quantitative agreement. Also, the normalized intensity of the skyrmion satellite peaks closely resembles the trends in the evolution of the electric-field dependence of the permittivity (dark gray, Supplementary Fig. 14e). The same trend is observed in the temperature-dependent change of effective dielectric permittivity of the superlattice (Supplementary Fig. 17) which closely follows the experimentally measured temperature-dependent permittivity.

Such polar skyrmions are characterized mathematically by the topological charge/number, $N_{\mathrm{Q}} = \frac{1}{4\pi}\iint \vec{u} \cdot \left(\frac{\partial \vec{u}}{\partial x} \times \frac{\partial \vec{u}}{\partial y}\right) dxdy$, where $\vec{u}$ denotes the normalized local dipole moment, and the surface integral is taken over the corresponding (001). The integrand is the Pontryagin density, and its surface integral is the topological number of the observed skyrmion, which takes an integer value of +1 as confirmed by phase-field and second-principles simulations.[1] Our simulations suggest a topological transition from a skyrmion state to uniform ferroelectric state at an electric field $\gtrsim$ 1500 kV/cm. Below this threshold, their Pontryagin density is finite (Supplementary Fig. 18) and the topological number remains +1 (Fig. 4g). Above this field, the skyrmion disappears indicating that the polarization texture is unstable and transforms to a uniform ferroelectric state with a trivial $N_{\mathrm{Q}} = 0$ (Fig. 4g and Supplementary Fig. 12-14). The application of thermal excitations also induces a similar topological-phase transition from the skyrmion state to a uniform ferroelectric state, with a phase-field estimated critical temperature of ~700 K. Experimentally,

such phase transitions can be inferred from the presence (skyrmion phase, $N_{\mathrm{Q}} = 1$) or absence (trivial topological phase, $N_{\mathrm{Q}} = 0$) of intensity in the side-lobe satellites in the electric-field- (Fig. 4f, g) or temperature- (Fig. 4h and Supplementary Fig. 17) dependent RSMs. The satellite peaks arising from the skyrmions disappear, respectively, at 1500 kV/cm and at ~600 K, indicating that the topological number switched from +1 to 0 (Supplementary Fig. 17); which, again, agrees qualitatively with the theoretical expectations. The field-driven change to the skyrmion is due to the shrinkage of the volume of the domain with a polarization opposite to the external electric field. For a critical field, the domain will collapse and the transition to a monodomain state is completed. Right before the transition, a singularity appears: the stereographic projection of the dipole pattern does not completely wrap the unit sphere. That is exactly the point where the skyrmion number changes from +1 (non-trivial topological structure) to 0 (trivial case in the monodomain configuration). Finally, such a field/temperature driven topological-phase transition bears resemblance to that in other topological structures (*i.e.*, magnetic field and temperature dependent phase transitions in magnetic skyrmions[4] and the corresponding field dependence of the magnetic susceptibility in them[31], phase transitions driven by chemical doping in spin textures[32], electric field in dipolar textures[33] and optical pulses in charge density wave systems).[34]

To further understand the reversible evolution of these structures under applied fields, the temporal evolution of the skyrmion ground state can be probed by perturbing it with electric-field pulses that drive the system to a uniform-polar state and then measuring the time-dependent evolution back to the skyrmion state (Fig. 5, Supplementary Fig. 19, 20, and Methods). Here, we focus on two sets of measurements. The first focuses on applying strong, unipolar pulses (U_1 and U_2) with varying lengths of delay time (t_d) between the pulses. We measure the current that flows

in the capacitor during the application of U_1 (*i.e.*, I_1), then allow possible relaxation to occur during t_d, and finally measure the current that flows during the application of U_2 (*i.e.*, I_2). Taking the difference I_1-I_2 for various t_d provides a time-dependent measure of the amount of relaxation after the poling process. For short-delay times ($t_d \lesssim 10$ μs; Fig. 5a) for a classical ferroelectric, there are two possible forms of response: 1) zero difference between I_1 and I_2 meaning the ferroelectric remains stable in the poled state with no relaxation (solid line, Fig. 5b) or 2) there is non-zero difference between I_1 and I_2 corresponding to a switching transient which occurs from (partial) relaxation (*i.e.*, back-switching) of the ferroelectric polarization during t_d (dashed line, Fig. 5b). When such an experiment is completed for the parent 50-nm-thick $PbTiO_3$ heterostructure (data here at t_d = 200 ns, Fig. 5c), a flat, zero response corresponding to stable, poled ferroelectric behavior is observed. On the other hand, similar experiments for the superlattices with skyrmions (data here at t_d = 200 ns, Fig. 5d) reveal a transient peak suggesting that there is a relaxation process different from what is observed in a classical ferroelectric based on the same material (data at other short t_d values is also provided, Supplementary Figure 20).

To further understand the relaxation processes, and in particular, reveal the time scales over which these processes persist, we carried out similar experiments with progressively longer t_d. Upon transitioning to long-delay times (10 μs $\lesssim t_d \lesssim$ 1 s, Fig. 5e) and again considering a classical ferroelectric there are two possible forms of response: 1) zero difference between I_1 and I_2 corresponding to the ferroelectric again remaining stable in the poled state with no relaxation (solid line, Fig. 5f) or corresponding to a ferroelectric that has completely back-switched such that the same large currents are measured under both U_1 and U_2 (long-dashed long, Fig. 5f) or 2) there is non-zero difference between I_1 and I_2 corresponding to a switching transient which occurs from partial back-switching of the ferroelectric polarization during t_d (short-dashed line, Fig. 5f). When

such an experiment is completed for the parent 50-nm-thick $PbTiO_3$ heterostructure (data here at t_d = 1 s, Fig. 5g), a flat, zero response corresponding to a stable, poled ferroelectric behavior is once again observed. Likewise, similar experiments for the superlattices exhibiting the skyrmion structures (data here at t_d = 1 s, Fig. 5h) reveal a flat, zero response suggesting the relaxation process has been completed within 1 s (data at other long t_d values is also provided, Supplementary Figure 20).

Thus far, the observations suggest that (not surprisingly) the single-layer parent ferroelectric film remains stable in whatever state it is electrically poled into, while the superlattices exhibiting skyrmion structures are found to exhibit relaxation processes. This could correspond to classical back-switching (*i.e.*, the applied bias pushes the skyrmion into a uniform polar state which then relaxes back to a classical up-and-down-poled domain structure) or could indicate a novel relaxation back towards the skyrmion structure. To differentiate between these two cases, a second set of experiments, wherein we apply a preset-pulse V opposite to U_1 and U_2 while focusing on long t_d (Fig. 5i), allows us to make this distinction. In the case of a classic ferroelectric there are again two possible types of response: 1) there is non-zero difference between I_1 and I_2 corresponding to a switching transient which occurs for the case of no back-switching since the preset-pulse V completely switches the material prior to U_1 and thus the response from U_1 to U_2 is different (solid line, Fig. 5j) or 2) zero difference between I_1 and I_2 meaning the ferroelectric completely back-switches after the preset-pulse V and between pulses U_1 and U_2 thus the difference in the response is the zero (dashed line, Fig. 5j). When such an experiment is completed for the parent 50-nm-thick $PbTiO_3$ heterostructure (data here at t_d = 1 s, Fig. 5k), a non-zero response, corresponding to what is expected for a stable, poled ferroelectric behavior is observed. This is in contrast to the data for the long-delay time studies without the preset pulse

which shows no peak (Fig. 5g). On the other hand, similar experiments for the superlattices exhibiting the skyrmion structures (data here at t_d = 1 s, Fig. 5l) reveal a small transient peak suggesting the ability to switch the small remnant polarization of these heterostructures (Supplementary Fig. 19). From other experiments (Fig. 5d and g), it appears that these superlattices are relaxing or back-switching within ~1 s; however, if this was true, we should have seen no peak in this preset-pulse experiment (Fig. 5l). Thus, this is indicative of a totally different relaxation process, *i.e.*, it cannot be explained simply by a classical back-switching of a ferroelectric, but instead suggests there is a novel, time-dependent evolution of the emergent polarization state such that we can unravel and then re-establish reversibly. This large, reversible field-dependent tunability arises from the ability of these emergent skyrmion structures to restore themselves to something akin to their original state upon turning-off the applied-electric field. The microscopic nature of this reversible recovery of the skyrmion state should be a matter of great interest for future studies.[35]

In summary, we have demonstrated that polar skyrmions in $(PbTiO_3)_n/(SrTiO_3)_n$ superlattices are comprised of a sheath with negative permittivity at the periphery of each skyrmion which enables a strong enhancement of the effective dielectric permittivity as compared to the individual $SrTiO_3$ and $PbTiO_3$ layers. This work has demonstrated a direct relationship between the macroscopically measured dielectric permittivity and the microscopically imaged potential energy landscape. Of greater importance is the observation that this same sheath is associated with the non-trivial topological number for each skyrmion. Application of an electric field drives the skyrmions into a uniform polar state with an accompanying large tunability of the permittivity as well as a corresponding topological phase transition, which is analogous to what is observed in the case of magnetic skyrmions and their magnetic field driven evolution into a uniform magnetic

state. Turning off the electric field, however, results in a time-dependent recovery of the skyrmion state (and dielectric response) suggesting the ability to unravel and reestablish these structures with electric field. The production of steady-state negative capacitance and large field-tunable response has promise for electronic applications.

METHODS

Sample preparation using RHEED-assisted pulsed-laser deposition

n-$SrTiO_3$/*n*-$PbTiO_3$/*n*-$SrTiO_3$ trilayers (*n*- is the number of monolayers) and $[(PbTiO_3)_n/(SrTiO_3)_n]_m$ (*n*- is the number of monolayers, *n*=8-16, *m*=3-8) superlattices were sandwiched by conducting 10 nm bottom $SrRuO_3$ and 60 nm top $SrRuO_3$. Trilayer and the superlattices were synthesized on TiO_2-terminated single-crystalline $SrTiO_3$ (001) substrates via reflection high-energy electron diffraction (RHEED)-assisted pulsed-laser deposition (KrF laser). The $PbTiO_3$ and the top $SrTiO_3$ were grown at 600 °C in 100 mTorr oxygen pressure. Growth temperature and oxygen pressure for the bottom $SrRuO_3$ layer were 700°C and 50 mTorr, respectively. For the top $SrRuO_3$ layer the corresponding parameters were 600°C and 100mTorr. For all materials, the laser fluence was 1.5 J/cm^2 with a repetition rate of 10 Hz. RHEED was used during the deposition to ensure the maintenance of a layer-by-layer growth mode for both the $PbTiO_3$ and $SrTiO_3$. The specular RHEED spot was used to monitor the RHEED oscillations. After deposition, the superlattices were annealed for 10 minutes in 50 Torr oxygen pressure to promote full oxidation and then cooled down to room temperature at that oxygen pressure.

Structural analysis

Laboratory-based X-ray diffraction: Structural characterization of the trilayer and superlattices were carried out using an X-ray Diffraction (XRD) diffractometer with Cu-K_α radiation (λ = 1.5405 Å). The high crystalline quality of the films, and the smooth nature of the interfaces were confirmed from θ-2θ symmetric XRD scans around the 002 reflection, which show strong superlattice peaks and Laue oscillations (not shown).

Synchrotron X-ray diffraction: In order to obtain a comprehensive picture of the structure, of the skyrmion in the trilayers and superlattices, as well as information on the in-plane and out-of-plane ordering and temperature dependent skyrmion structures, further structural characterization was performed using synchrotron-based XRD with monochromatic hard X-ray beams at 10 keV to 25 keV at the 33-BM-C, 33-ID-B, 7-ID-C and 12-ID-B beamlines of the Advanced Photon Source (APS), Argonne National Laboratory, USA. The Huber and Newport diffractometers used at APS allows us to determine the orientation of our crystals reliably, and to obtain 3-dimensional reciprocal space mappings based on rocking scan sampling with high angular accuracy. The high flux from the synchrotron X-ray source delivered at these beamlines allows one to detect the weak diffracted intensities arising from the lattice modulations associated with the polar-skyrmion bubbles present in the $(PbTiO_3)_n/(SrTiO_3)_n$ superlattices.

Macroscopic capacitance measurement

Out-of-Plane Measurements: In order to measure the electrical properties of the superlattices circular capacitor structures of 25 μm, 50 μm, 100 μm diameter were fabricated using pulsed laser deposition followed by photolithography and etching. The fabrication is comprised of three processes: a) etching, b) lift-off and c) shadow mask deposition. At first photolithography was used to define the photoresist layer. Dry etching was carried out by Ar ion beam milling at 1×10^{-4} Torr Ar pressure at a rate of 6 nm/min to remove the top electrode layer. Temperature dependent small signal ac permittivity was measured using an E4990A Impedance Analyzer using an a.c. excitation voltage of 10mV at various frequencies.

In-plane Measurements: A transmission-line approach was used to measure the in-plane dielectric properties of a $[(PbTiO_3)_{16}/(SrTiO_3)_{16}]_8$ superlattice at microwave frequencies from 100 MHz to 10 GHz. To perform these measurements, an array of eight gold co-planar waveguide (CPW) transmission lines ranging in length from 0.42 mm to 6.60 mm were patterned on the surface of the superlattice film using standard lift-off fabrication techniques (Supplementary Figure 9a). The center conductor of the CPWs was 20 μm wide and was separated from 150 μm-wide ground planes by a 5 μm wide gap. An identical pattern was also fabricated on a bare $SrTiO_3$ (001) substrate for reference. The dimensions of the devices were measured using optical microscopy and profilometry, and the conductivity of the gold was obtained from DC resistance measurements.

The scattering (S-) parameters of the transmission line devices were then measured at room temperature from 100 MHz to 10 GHz using a vector network analyzer (VNA) at a power of -15 dBm and an IF bandwidth of 30 Hz. The VNA was calibrated using custom-fabricated on-wafer calibration standards with device geometries consistent with the devices on the superlattice film and bare substrate. The NIST StatistiCal software package was used to implement the multiline-TRL algorithm [B1, B2] to extract accurate estimates of the propagation constant, γ, from the S-parameter measurements of the CPWs on the superlattice film and bare substrate. The propagation constant is related to the distributed circuit parameters of the CPW by the relationship $\gamma = \sqrt{R + i\omega L}\sqrt{G + i\omega C}$, where *R*, *L*, *G,* and *C* are the distributed resistance, inductance, conductance and capacitance per unit length, respectively, and ω is the angular frequency. These circuit parameters are related to the geometries and material properties of the metal layers comprising the CPW, and the surrounding dielectric layers, which are probed by electric fields generated in the devices during measurement (Supplementary Figure 9b). If *R* and *L* are known, *C* and *G*, which are proportional to the real and imaginary parts of the effective permittivity, respectively, can be

extracted from γ. In the devices on the superlattice film chip, the in-plane electric fields interact with both the superlattice film and the substrate, therefore some portion of the overall measured *C* and *G* can be attributed to the permittivity of the film (C_{FILM}, G_{FILM}), and to the permittivity of the substrate (C_{SUB}, G_{SUB}) as illustrated in the stylized circuit model for these transmission lines (Supplementary Figure 9c). The measurement of the bare substrate is used to aid in separating these contributions to the overall measurement. Finite element simulations of the device structures incorporating the measured dimensions and metal properties were generated and validated by comparison to known devices. These simulations are first used to obtain the *R* and *L* values for the CPW devices in order to extract *C* and *G*, and finally are used to obtain the mapping function relating *C* and *G* to the real (ε_1) and imaginary (ε_2) parts of the permittivity, respectively.

***In-situ* electric field dependent structural measurements**

Synchrotron X-ray diffraction measurements as a function of electric field (applied voltage divided by the thickness of the sample) were conducted at the 7-ID-C, 32-ID-B and 12-ID-B beamlines at APS using $(PbTiO_3)_n/(SrTiO_3)_n$ superlattice samples deposited on (100) $SrTiO_3$ substrates, n=16, 20 and total superlattice thickness of ~ 100 nm. By employing capacitor device geometry with superlattice sandwiched between $SrRuO_3$ electrodes grown at the substrate interface and on top of the superlattice stack, additional *in-situ* electric-field-dependent measurements of superlattices were performed at 7-ID-C and 32-ID-B beamlines. In a first device geometry used at sector 32-ID-B, the incident X-ray beam at 10 keV was focused using two Kirkpatrick-Baez (KB) mirrors to a spot of ~ 30 μm x 90 μm on the top electrode of a capacitor device with a lateral size of 150 μm x 150 μm. To study the effect of out-of-plane electric field, a constant dc voltage was applied to the capacitor device, while the intensity of various peaks was monitored with a gated area

detector, which acquired the distribution of scattered X-ray intensity in reciprocal space, followed by reciprocal space mapping reconstruction. Device to device data reproducibility was additionally checked at sector 7-ID-C using several capacitor devices with 25 μm diameter and a 11 keV X-ray beam focused by a zone-plate to ~ 1 μm x 1 μm on the top of the capacitors. On these smaller capacitors, the electric field application was initiated using a sharp Pt tip of a few nm's in size placed in contact with the top electrode under a nanoscale probe imaging station called XSNOM (X-ray Scanning Near-field Optical Microscope).[36]

Mesoscopic model for negative permittivity calculation of the skyrmion

We describe an effective permittivity model to study the local negative capacitance/permittivity of the $PbTiO_3/SrTiO_3$ superlattices containing polar skyrmions. It is important to make the distinction between local and global capacitance as a local negative capacitance is permitted if overall capacitance $C_{eff} > 0$ is satisfied, while $C_{eff} < 0$ is not allowed from minimum energy principles, as shown in Fig.2d. One particular point of interest is the enhancement in the capacitance that one acquires in the presence of a local negative capacitance/permittivity. Negative capacitance can be realized in regions with intermediate polarization between two equilibrium polar states, e.g., in the vicinity of a domain wall or polar vortex core.[3] In a $[(PbTiO_3)_{16}/(SrTiO_3)_{16}]_8$ superlattice, the presence of domain wall-like polar skyrmions gives rise to local negative dielectric permittivity, and thus a much higher effective dielectric permittivity of the superlattice. Based on the measured dielectric constant of $\varepsilon_{eff} = 800$, we can estimate the dielectric constants of the individual layers, by modeling our superlattice as capacitors in series. As denoted from Fig.2d, the "bulk" region is marked as A_2 (yellow), while A_3 represents the area of a skyrmion wall (blue), where the ratio of the "wall" region is approximately 31%. A_1 corresponds to the area of $SrTiO_3$ layers. We assign

the dielectric constants of $SrTiO_3$, $PbTiO_3$ (domain) and $PbTiO_3$ (wall) to be $\varepsilon_{1,}$ ε_2 and ε_3, respectively.

Using a capacitor model, the effective dielectric capacitance can be expressed as

$$\frac{1}{C_{Eff}} = \frac{8(16)}{C_1} + \frac{8(16)}{C_2} = \frac{8(16)C_2 + C_1 8(16)}{C_1 C_2}$$

The capacitance of a $PbTiO_3$ layer is

$$C_2 = \sum_{i=1}^{n} C_{2_i} + C_{3_i}$$

where the summation corresponds to n number of parallel capacitors $C_2,\ C_3$). In general,

$$C = \frac{KA}{D}$$

where *K* is permittivity of the layer, *A* is area of the layer, *D* is thickness of the layer. Therefore, we can rewrite the capacitances in terms of dielectric constants as

$$\frac{\varepsilon_{eff} A_{eff}}{D_{Eff}} = \frac{\frac{\varepsilon_1 A_1}{D}\left(\sum_{i=1}^{n} \frac{\varepsilon_{3_i A_{3_i}}}{D} + \frac{\varepsilon_{2_i A_{2_i}}}{D}\right)}{8(16)\left(\sum_{i=1}^{n} \frac{\varepsilon_{3_i A_{3_i}}}{D} + \frac{\varepsilon_{2_i A_{2_i}}}{D}\right) + 8(16)\frac{\varepsilon_1 A_1}{D}}$$

We can drop the summation sign by assuming that every ε_{3_i} is of equal dielectric constant allowing us to write $\varepsilon_3 \sum_{i=1}^{n} A_{3_i}$. By examining the planar section (Fig.2a and Supplementary Fig. 1b), $\sum_{i=1}^{n} A_{3_i}$ is estimated to be approximately 31% of A_1 where A_1 is the total area of our map. Likewise, $\sum_{i=1}^{n} A_{2_i}$ is approximately 69 % of A_1. In addition, D_{eff} is simply $16(16)D$, where $A_{eff} = 8(16)A_1 + 8(16)A_2$. The A_2 is simply the summation, $\sum_{i=1}^{n} A_{2_i} + A_{3_i} = A_1$, hence $A_{eff} = 8(16)A_1 + 8(16)A_2 = 16(16)A_1$. Putting them all together we have,

$$\frac{\varepsilon_{Eff} 16(16) A_1}{16(16)D} = \frac{\frac{\varepsilon_1 A_1}{D}\left(\frac{\varepsilon_2 0.69 A_1}{D} + \frac{\varepsilon_3 0.31 A_1}{D}\right)}{(16)8\frac{\varepsilon_1 A_1}{D} + 8(16)\left(\frac{\varepsilon_2 0.69 A_1}{D} + \frac{\varepsilon_3 0.31 A_1}{D}\right)}$$

or

$$\varepsilon_{eff} = \frac{\varepsilon_1(\varepsilon_2 0.69 + \varepsilon_3 0.31)}{(16)8\varepsilon_1 + 8(16)(\varepsilon_2 0.69 + \varepsilon_3 0.31)}$$

We can solve the above equation for ε_3,

$$\varepsilon_3 = \frac{\varepsilon_1\varepsilon_2 0.69 - \varepsilon_{eff}\varepsilon_1(128) - \varepsilon_{eff}\varepsilon_2(0.69)128}{\varepsilon_{eff}128(0.31) - \varepsilon_1 0.31}$$

From the above equations, in the classical situation, several capacitors in series will result in a total/effective capacitance smaller than that of each individual capacitor as shown in Fig.2f (black horizontal line in Fig.1a). Taking the dielectric permittivity of the skyrmion wall as $\varepsilon_3 = 1000$ will give an effective permittivity $\varepsilon_{eff} = 8$ which agrees with the classical result, but did not agree with the measured effective dielectric permittivity 800. On the other hand, to obtain a $\varepsilon_{eff} = 800$ we plotted ε_3 with respect to different $\varepsilon_1, \varepsilon_2$ (Fig.2e). It can be seen that it is only possible to achieve the experimentally measured superlattice dielectric permittivity by having a negative permittivity in the skyrmion "wall" regions.

Phase-field modeling

To predict and understand the structures and responses of the polar skyrmions under applied electric and thermal stimuli, phase-field simulations were performed for the $(PbTiO_3)_{16}/(SrTiO_3)_{16}$ superlattice on a $SrTiO_3$ substrate by evolving spatial distributions of polarization vector $\vec{P}$, strain, and electric potential (and thus electric field). [1, 2, 37]

$$\frac{\partial P_i}{\partial t} = -L\frac{\delta F}{\delta P_i} (i=1, 3)$$

where t is the simulation time step, and L is the kinetic coefficient related to the bulk domain wall mobility.

The total free energy F of the superlattice contains contributions from mechanical, electrostatic, Landau chemical and polarization gradient energies:

$$F = \int_V (f_{mech} + f_{elec} + f_{Land} + f_{grad}) dV$$

The detailed expressions of the energy densities and the material parameters can be found elsewhere.[38,39] The simulation cell is discretized into 3-Dimensional grids of 200 x 200 x 350, with each grid representing 0.4 nm. Periodic boundary conditions are applied along the in-plane dimensions while a superposition scheme[37] is imposed along the thickness dimension which is composed of 30 grids of substrate, 288 grids of thin film layers (which is consisting of repeating units of 16 $PbTiO_3$ layers and 16 $SrTiO_3$ layers) and 32 grids of vacuum. The thin film boundary condition is applied where it is stress free on the top of the film and the displacement is zero on the bottom of the substrate sufficiently far away from the substrate/thin film interface.[37] An iteration-perturbation method is used to account for the elastic inhomogeneity of the two materials.[37]

The local electric potential φ can be obtained by solving the Poisson's equation[37]: $\varepsilon_0 K_{ij} \frac{\partial^2 \varphi}{\partial x_i x_j} = P_{i,i}$, where ε_0 is the permittivity of vacuum, K_{ij} is the background dielectric constant.[36] The electric field E_i can be expressed by the gradient of the electric potential, i.e., $E_i = -\nabla_i \varphi$. A close-circuit electric boundary condition[37] is used with the electric potential both at the bottom and top of the thin film set to be zero or a specified applied potential. The polar skyrmion array[1] is stabilized at room temperature, starting from initial random noise, which is used for the follow-up calculations. The macroscopic dielectric constant at the given electric potential bias is calculated by giving small potential perturbations: $\square_{33} = \frac{\square \langle P_3 \rangle d}{\varepsilon_0 \square \phi} + K_{33}$, d is the thickness of the thin film. While the spatially resolved local permittivity[3] is defined as: $\square_{33} = \frac{\Delta P_3}{\varepsilon_0 \Delta E_3} + K_{33}$. The thermal stability of the polar skyrmion is also investigated in the temperature range of 300 K to 800 K. Since, $PbTiO_3$ and $SrTiO_3$ have similar thermal expansion coefficients, the substrate strain

is assumed to be constant across the whole temperature range. The lower bound of the transition temperature is estimated by adding a 0.05% relaxation of the substrate strain (which is the uncertainty of the measurement). The switching kinetics are also studied with an applied field in the range from -1500 kV/cm to +1500 kV/cm.

Second-principles calculations

The second-principles simulations have been performed using the same methodology presented in previous works[1,40,41,42] as implemented in the SCALE-UP package.[40] The interactions inside the $PbTiO_3$ or $SrTiO_3$ are described using the potentials for the bulk materials.[41] These potentials give qualitatively correct descriptions for the lattice dynamical properties and structural phase transitions of both materials. Then, we treat the interactions at the interface between $PbTiO_3$ and $SrTiO_3$ assuming a simple numerical average for the interactions of the ions pairs touching or crossing the interface. The main effect of the stacking is electrostatic wherein long-range dipole-dipole interactions are governed by a bare electronic dielectric constant ε_∞ that is taken as a weighted average of the first-principles results for bulk $PbTiO_3$ ($8.5\varepsilon_0$) and $SrTiO_3$ ($6.2\varepsilon_0$), with weights reflecting the composition of the superlattice. To preserve the electrostatic energy within each material as close as possible to the bulk parent compounds, the Born effective charge tensors of the inner atoms were rescaled by $\sqrt{\varepsilon_\infty}/\varepsilon_\infty^{ABO_3}$ (where ABO_3 stands for $PbTiO_3$ or $SrTiO_3$ depending on the layer).

The second-principles parameters of both materials were fitted from density functional theory imposing a hydrostatic pressure of -11.2 GPa to counter the underestimation of the local density approximation (LDA) of the cubic-lattice constant that was taken as the reference structure.

We impose an epitaxial constraint assuming in-plane lattice constants of a=b=3.901 Å, forming an angle γ=90°, which corresponds to a SrTiO3 (001)-oriented substrate.

Following this strategy, we are able to construct models for superlattices with arbitrary n stacking. For the simulations, we used periodically repeated supercells that contain 20×20 elemental perovskites units in-plane, and one full superlattice period in the out-of-plane direction. To solve the models, we have used standard Monte Carlo and Langevin molecular-dynamics methods; at low temperature only random configurations along the Markov chains that produce a lowering in the energy are accepted. By following this procedure as an equivalent to structural relaxations we find the ground state. The local polarizations were obtained within a linear approximation, computing the product of the atomic displacements from the reference structure, that correspond to the ideal cubic perovskite, times the Born effective charge tensor divided by the volume of the unit cell. The skyrmion number, N_{SK}, was obtained from the local dipoles computing the normalized polarization field defined along each slice of 20×20×1 elemental perovskite unit in-plane of our supercell and solving the Eq. (1), obtaining a skyrmion number that corresponds to an integer number.[1,43]

Finally, the local dielectric constant and the electric susceptibilities were computed following the strategy presented in ref. 3. There the inverse of the dielectric constant was defined to be a measurement of the change in the local electric field with the variation of the electrical boundary conditions that sets the macroscale electric displacement vector. The normal component of the displacement electric field can be monitored by the external electric field. In the same spirit, the local electric susceptibilities measure the changes in the local polarization under the application of the same external electric field.

To compute the global dielectric permittivity, the skyrmion structure was relaxed under different external electric fields of increasing magnitude. The starting configuration for a given value of the external field was the relaxed structure obtained for the former field. After relaxation, the global polarization along the *z*-direction was averaged for the whole supercell. From the plot of P_z versus the external field, a fit to a Landau-type equation of state was performed, including up to five order terms. Finally, the global electronic susceptibility was estimated as $\epsilon_z = 1 + \frac{1}{\epsilon_0}\frac{\partial P_z}{\partial E_{\text{ext},z}}$.

SCBED for local potential energy measurement

Scanning convergent beam electron diffraction (SCBED) experiments were performed using an electron microscopy pixel array detector (EMPAD) and a TEM operated at 300 keV with 15 pA beam current, 2.0 mrad semi-convergence angle, having a probe of ~8 Å FWHM (full-width at half-maximum). The CBED patterns were captured by the EMPAD with exposure time set to 1 ms per frame. The TEM specimen has a thickness of ~25 nm as determined by CBED simulations using EMPAD. Cross-sectional measurements enable access to the cross-section of the Bloch component of the skyrmions away from the interfaces, where the technique is most robust.

Both ferroelectric polarization and electric field need to be measured independently and simultaneously to extract local potential energy. First, long-range electric fields can be reconstructed from the deflection of the entire CBED pattern due to the Lorentz force[29, 30]. For this study, we focused on the deflection of (000) beam as there are fewer polarity effects. Secondly, due to dynamical diffraction effects, the polarization direction can be retrieved from the diffraction intensity differences of Friedel pairs, such as (100)/($\bar{1}$00) and (001)/(00$\bar{1}$) for the x and z

components of polarity, respectively. We carefully selected local regions with minimal tilt and thickness variations, as these effects complicate the analysis and give rise to nontrivial artefacts. Now that both electric field and polarization field are measured, we can thus calculate local potential energy of the system.[2] We have,

$$dG = EdP \qquad (1).$$

For a cross section geometry (*xz*-plane), we can derive the internal energy by integration

$$G = \int (E_x \partial_x P_x + E_z \partial_z P_x) dx + \int (E_x \partial_x P_z + E_z \partial_z P_z) dy \qquad (2).$$

Based on the analysis (Fig.3), the potential energy has local maxima at the domain walls, where the out-of-plane polarization (z component) was suppressed.

Probing the transient capacitance state

We apply a series of two identical, consecutive (U_1 and U_2 in Fig.4a) unipolar pulses with a pulse width of 10 μs to the sample. Each pulse generates a field of 1300kV/cm in the film. During each pulse, we monitor the current through the sample. The time delay between pulses is variable, given by t_d. During the delay time, no electric field is applied and the system begins to relax to the ground (skyrmion) state. U_2 probes the capacitance *at the time of application,* and as such by varying t_d and comparing the currents I_1 and I_2 generated in the circuit in response to the pulses U_1 and U_2, we can probe the evolution of the sample back toward the ground state. Upon subtracting the response (*i.e.,* I_2) to pulse U_2 from the response (*i.e.,* I_1) to pulse U_1, we observe a discernable difference between the response to poling pulse (U_1) and the following pulse (U_2) (Fig.4). This difference is attributed to the formation of a transient capacitive state where the system is driven out of equilibrium (toward the uniform polarization state) and then relaxes back to the ground state. The difference between U_1 and U_2 is largest for short delay times, t_d, and decays with longer

delay times, as is expected while the transient state decays. This difference could be attributed to back-switching of the small remnant polarization of the sample, however a similar experiment which includes a preset down pulse reveals that this cannot be the case (Fig. 5).

Acknowledgements

This work is supported by the Quantum Materials program from the Office of Basic Energy Sciences, US Department of Energy (DE-AC02-05CH11231) (S.D., M.R.M. and R.R.). M.A.P.G. and J.I are funded by the Luxembourg National Research Fund through the CORE program (Grant FNR/C15/MS/10458889 NEWALLS). L.-Q.C and L.W.M. acknowledge support from the U.S. Department of Energy, Office of Science, Office of Basic Energy Sciences, under Award Number DE-SC-0012375 for the development and study of novel ferroic heterostructures. Additional work at Penn State further acknowledges the National Science Foundation under grant DMR-1744213 and the Extreme Science and Engineering Discovery Environment (XSEDE) cluster, which is supported by National Science Foundation grant number ACI-1548562, and specifically, it used the Bridges system, which is supported by NSF award number ACI-1445606, at the Pittsburgh Supercomputing Center (PSC)[44,45] , under the allocation DMR170006. Z.H. acknowledges support from the National Science Foundation under grant DMR-1210588. F.G.O, P.G.F. and J.J. acknowledge financial support from the Spanish Ministry of Economy and Competitiveness through grant number FIS2015-64886-C5-2-P and PGC2018-096955-B-C41, and P.G.F. acknowledges support from Ramón y Cajal grant No. RyC-2013-12515. J.W.F. and V.A.S acknowledge support from the U.S. Department of Energy, Office of Science, Office of Basic Energy Sciences, under Award Number DE-SC- 0012375. V.A.S., M.R.M, S.D., H.W., Z.Z., J.W.F. and H.Z. acknowledge use of the Advanced Photon Source, a U.S. Department of Energy (DOE) Office of Science User Facility operated for the DOE Office of Science by Argonne National Laboratory under Contract No. DE-AC02-06CH11357. V.A.S. and H.W. would like to thank to Qian Li and Samuel Marks for kind assistance in operating the XNOM station at 7-ID-C beamline of APS. Y.T.S. and D.A.M. acknowledge support from the AFOSR Hybrid Materials

MURI, under award number FA9550-18-1-0480. We acknowledge the electron microscopy facility from the National Science Foundation (DMR-1719875 and DMR-1429155). E.J.M., C.J.L., N.D.O. acknowledge to J.C. Booth for establishing the high frequency testing facility at NIST, funding E.J.M., and developing the original on-wafer techniques.

Author Contributions

S.D. and R.R. designed the experiments. S.D. carried out the synthesis and characterization of trilayers and superlattice samples. S.D. carried device fabrication on this samples and S.D. and S.S. performed all macroscopic electrical measurements. Y.T.S. performed EMPAD characterization of the samples under the supervision of D.A. M. M. A. P. G, F.G.O, P.G.F, J. Í. and J.J. completed the second-principles simulations. Z.H. performed and analyzed phase-field calculations for these samples. V.A.S., M.R.M. and S.D. did the reciprocal space map studies of these samples using lab x-ray diffraction and synchrotron X-ray diffraction. V.A.S. carried out the electric field dependent reciprocal space map studies of these samples using synchrotron X-ray diffraction. E.P. and S.D. performed electric field dependent of pulse dynamics. E.J.M designed the layout, fabricated the in-plane devices and performed the microwave measurements, analyzed the data and wrote microwave section. N.D.O. and A.M.H. supervised the microwave research and N.D.O. wrote the algorithms that calibrated and processed the data, wrote the analysis tools. C.J.L. wrote the algorithms that generated the layout, optimized the devices performance, and calibrates and processes the data. S.D. Z.H. V.A.S., S.S., J.J., L.Q.C., and R.R. analyzed the data and co-wrote the manuscript. R.R., L.Q.C., L.W.M., S.S. and J.J. supervised the research. All authors contributed to the discussion and manuscript preparation.

Competing financial interests

The authors declare no competing financial interests.

Copyright Disclaimer

References

[1] Das, S et al. Observation of room temperature polar skyrmions. *Nature* **568**, 368-372 (2019).

[2] Yadav, A. K. et al. Spatially Resolved Steady State Negative Capacitance. *Nature* **565**, 468-471 (2019).

[3] Kosterlitz, J. M. and Thouless, D. J., Ordering, metastability and phase transitions in two-dimensional systems, *J. Phys. C: Solid State Phys*. **6,** 1181-1203 (1973).

[4] Nagaosa, N. and Tokura, Y., Topological properties and dynamics of magnetic skyrmions. *Nat. Nanotechnol*. **8**, 899-911 (2013).

[5] Rößler, U.K., Bogdanov, A.N., & Pfleiderer, C. Spontaneous skyrmion ground states in magnetic metals. *Nature* **442**, 797 (2006).

[6] Mühlbauer, S., Binz, B. *et al.,* Skyrmion Lattice in a Chiral Magnet. *Science* **323**, 915 (2009).

[7] Nahas, Y., Prokhorenko, S., Louis, L., Gui, Z., Kornev, I. & Bellaiche, L. Discovery of stable skyrmionic states in ferroelectric nanocomposites. *Nat. Commun.* **6**, 8542 (2015).

[8] Zhang, Q. et al. Nanoscale bubble domains and topological transitions in ultrathin ferroelectric films, *Adv. Mater.* **172**, 375 (2017).

[9] Gregg, J. M. Exotic domain states in ferroelectrics: searching for vortices and skyrmions. *Ferroelectrics* **433**, 74–87 (2012).

[10] Naumov, I. I., Bellaiche, L. & Fu, H. Unusual phase transitions in ferroelectric nanodisks and nanorods. *Nature* **432**, 737–740 (2004).

[11] S .Salahuddin and S.Datta, Use of negative capacitance to provide voltage amplification for low power nanoscale devices, *Nano Lett.* **8**, 405 (2008).

[12] S. Salahuddin and S. Datta, "Can the subthreshold swing in a classical FET be lowered below 60 mV/decade?," in Electron Devices Meeting, 2008. IEDM 2008. IEEE International, pp. 1–4, IEEE, 2008.

[13] T. N. Theis and P. M. Solomon, It's time to reinvent the transistor!, *Science*, **327**, 1600 (2010).

[14] Zubko, P. et al. Negative capacitance in multidomain ferroelectric superlattices. *Nature* **534**, 524, (2016).

[15] Appleby, D. J., Ponon, N. K., Kwa, K. S., Zou, B., Petrov, P. K., Wang, T., Alford, N. M., and O Neill, A., Experimental observation of negative capacitance in ferroelectrics at room temperature, *Nano Lett*., **14**, 3864 (2014).

[16] Íñiguez, J., Zubko, P., Luk'yanchuk, I., Cano, A., Ferroelectric negative capacitance. *Nat. Rev. Mater.* 4, 243–256 (2019).

[17] Hoffman, M. et al. Unveiling the double-well energy landscape in a ferroelectric layer. *Nature* **565**, 464-467 (2019).

[18] Bratkovsky, A.M., Levanyuk. A.P. Depolarizing field and "real" hysteresis loops in nanometer-scale ferroelectric films. *Appl. Phys. Lett.* **89**, 253108 (2006).

[19] Wang, X. et al, Van der Waals negative capacitance transistors. *Nat. Commun.* **10**, 3037 (2019).

[20] Lines, M. E. & Glass, A. M. Principles and Applications of Ferroelectrics and Related Materials (Clarendon Press, Oxford, 1977)

[21] Wu, X., Yang, E. S., and Evans, H. L. Negative capacitance at metal-semiconductor interfaces. *J. Appl. Phys.* **68**, 2845 (1990).

[22] Hoffman, M. et al, Ferroelectric negative capacitance domain dynamics. *J. Appl. Phys.* **123**, 184101 (2018).

[23] Damodaran, A. R. et al. Large polarization gradients and temperature-stable responses in compositionally-graded ferroelectrics. *Nat. Commun.* **8**, 14961 (2017).

[24]O'Neill, D., Bowman, R.M., Gregg, J.M. Dielectric enhancement and Maxwell–Wagner effects in ferroelectric superlattice structures. *Appl. Phys. Lett.* **77**, 1520 (2000)

[25] Catalan, G., O'Neill, D., Bowman, R.M., Gregg, J.M. Relaxor features in ferroelectric superlattices: A Maxwell–Wagner approach. Appl. Phys. Lett. **77**, 3078 (2000)

[26] Arai, H. *et al,* Fundamental Characteristics of Superconducting Fault Current Limiter Using LC Resonance Circuit. IEEE Transactions on Applied Superconductivity 16, 642-645 (2006)

[27] Kittel, C. Introduction to Solid State Physics (Wiley, Hoboken, 1966)

[28] Watanabe, Y. in Ferroelectric Thin Films: Basic Properties and Device Physics for Memory Applications (eds Okuyama, M. & Ishibashi, Y.) 177–199 (Springer, Berlin, 2005).

[29] Zubko, P., Stucki, N., Lichtensteiger, C., and Triscone, J.-M., X-Ray Diffraction Studies of 180º Ferroelectric Domains in $PbTiO_3/SrTiO_3$ Superlattices under an Applied Electric Field. *Phys. Rev. Lett.* **104**, 187601 (2010).

[30] Boulle, A., Infante, and Lemée, N. Diffuse X-ray scattering from 180 ferroelectric stripe domains: polarization-induced strain, period disorder and wall roughness. *J. Appl. Cryst*. **49**, 845–855 (2016).

[31] Okamura et al. Transition to and from the skyrmion lattice phase by electric fields in a magnetoelectric compound. Nat. Commun. **7**, 12669 (2016).

[32] Fujishiro *et al*. Topological transitions among skyrmion- and hedgehog-lattice states in cubic chiral magnets. Nat. Commun. **10**, 1059 (2019)

[33] Yang *et al*. Electric field driven evolution of topological domain structure in hexagonal manganites. Phys. Rev. B **96**, 144103 (2017)

[34] Zong *et al*. Evidence for topological defects in a photoinduced phase transition. Nat. Phys. **15** 27 (2019)

[35] Schulz, A., Ritz, R., Bauer, A., Halder, M., Wagner, M., Franz, C., Pfleiderer, C., Everschor, K., Garst, M., and Rosch, A. Emergent electrodynamics of skyrmions in a chiral magnet. Nature Physics **8**, 301-304 (2012).

[36] Li, Q. *et al*, Simultaneous scanning near-field optical and X-ray diffraction microscopy for correlative nanoscale structure–property characterization, J. Synchrotron Rad. **26**, 1790 (2019).

[37] Chen, L.-Q., Phase-Field Method of Phase Transitions/Domain Structures in Ferroelectric Thin Films: A Review. *J. Am. Ceram. Soc*. **91**, 1835 (2008).

[38] Sheng, G., Li, Y.L., Zhang, J.X., A modified Landau–Devonshire thermodynamic potential for strontium titanate. *Appl. Phys. Lett.,* **96**, 232902 (2010).

[39] Tagantsev, A. *et al.*, Landau Expansion for Ferroelectrics: Which Variable to Use? *Ferroelectrics,* **375**, 19-27 (2008).

[40] Wojdeł, J. C., Hermet, P., Ljungberg, M. P., Ghosez, P. & Íñiguez, J. First- principles model potentials for lattice-dynamical studies: general methodology and example of application to ferroic perovskite oxides. *J. Phys.: Condens. Matter* **25,** 305401 (2013).

[41] Wojdeł, J.C. and Íñiguez, J., Ferroelectric transitions at ferroelectric domain walls found from first-principles. *Phys. Rev. Lett.* **112**, 247603 (2014).

[42] Gonçalves, M. A. P. *et* al, Theoretical guidelines to create and tune electric skyrmion bubbles. *Science Advances* **5**, no. 2, eaau7023 (2019).

[43] B. Berg, B and Lüscher, M. Definition and statistical distributions of a topological number in the lattice O(3) σ-model, *Nucl. Phys. B* **190**, 412-424 (1981).

[44] Towns, J., Cockerill, T., Dahan, M., Foster, I., Gaither, K., Grimshaw, A., Hazlewood, V., Lathrop, S., Lifka, D., Peterson, G.D., Roskies, R., Scott, J.R. and Wilkens-Diehr, N. 2014. XSEDE: Accelerating Scientific Discovery. Computing in Science & Engineering. 16(5):62-74.

[45] Nystrom, N. A., Levine, M. J., Roskies, R. Z., and Scott, J. R. 2015. Bridges: A Uniquely Flexible HPC Resource for New Communities and Data Analytics. In Proceedings of the 2015 Annual Conference on Extreme Science and Engineering Discovery Environment (St. Louis, MO, July 26-30, 2015). XSEDE15. ACM, New York, NY, USA.

B1. Marks, R. B., A multiline method of network analyzer calibration. *IEEE Trans. Microw. Theory Tech.* **39**, 1205-1215 (1991).

B2. Williams, D. F., Wang, J. C. M. & Arz, U. An optimal vector-network analyzer calibration algorithm. *IEEE Trans. Microw. Theory Tech.* **51**, 2391-2401 (2003).

Figures and Captions

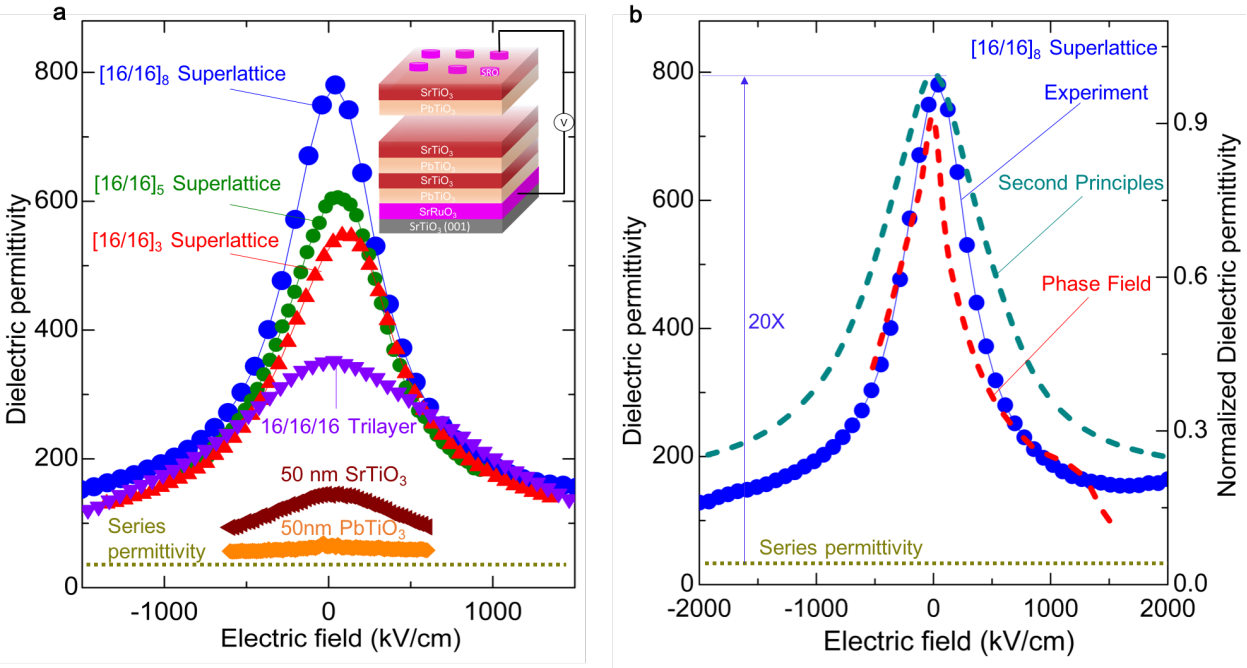

Figure 1| Macroscopic demonstration of stabilization in the negative capacitance of polar skyrmion. a, The dielectric permittivity as a function of electric field (applied voltage divided by the thickness of the sample) for $[(SrTiO_3)_{16}/(PbTiO_3)_{16}]_8$, $[(SrTiO_3)_{16}/(PbTiO_3)_{16}]_5$, $[(SrTiO_3)_{16}/(PbTiO_3)_{16}]_3$ superlattice and $(SrTiO_3)_{16}/(PbTiO_3)_{16}/(SrTiO_3)_{16}$ trilayer which is in skyrmion states compared to its constituents (50nm $SrTiO_3$ and 50 nm-thick $PbTiO_3$ layer). The horizontal dotted yellow line shows the effective permittivity at zero field (~37) from the series combination of effective 50nm $SrTiO_3$ and 50nm $PbTiO_3$ layers. Inset: schematic of the sample measurement geometry. **b,** Left axis: experimentally measured effective dielectric permittivity

(blue dots) as a function of electric field manifests itself in the enhancement of dielectric permittivity of the $[(SrTiO_3)_{16}/(PbTiO_3)_{16}]_8$ superlattice compared to the series permittivity (horizontal dotted yellow line) at zero field (~37). An enhancement in permittivity of almost ~20X is observed compared to this threshold, caused by a stabilized negative capacitance (permittivity) in the $PbTiO_3$ layer. Right axis: The normalized dielectric permittivity calculated from phase field (red dashed) and second-principles (green dashed) simulations closely resembles with the experimentally measured normalized electric-field dependence permittivity (blue dots). The results have been rescaled and the normalization is done with respect to the zero-field value.

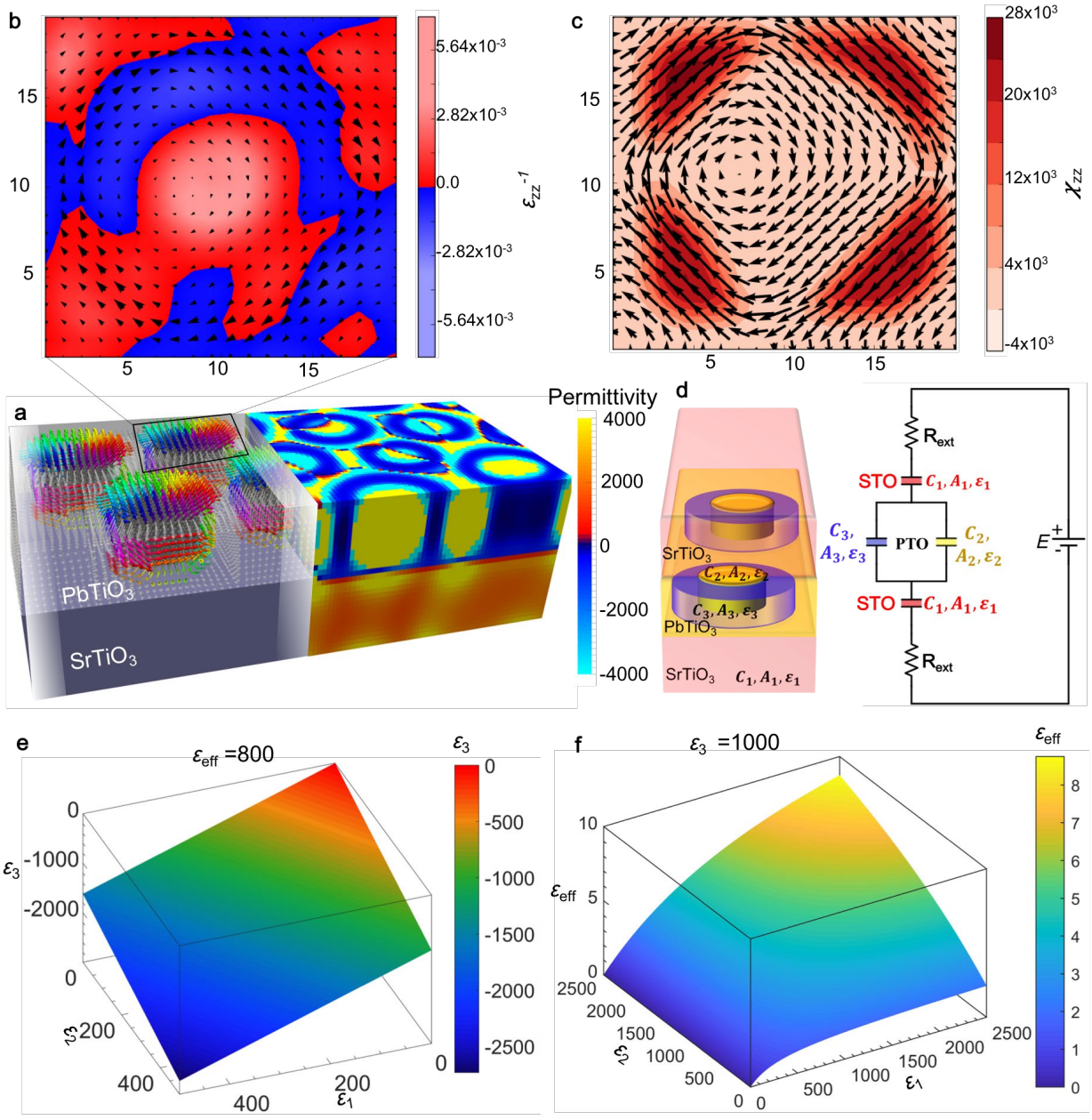

Figure 2| Phase field, second-principles and macroscopic calculations of negative permittivity of the skyrmion structure at 300 K in a $PbTiO_3$–$SrTiO_3$ superlattice. a, Left: second-principles calculations of the skyrmion structure in the superlattice. Right: phase field simulated spatial map of the permittivity of the central unit cell within the $PbTiO_3$ layer and presents the evidence of regions where the local permittivity is negative, shown in blue contrast. Second principles calculations of the two-dimensional distribution of **b,** the inverse of the

dielectric permittivity and **c,** the susceptibility at the central plane of $PbTiO_3$, that shows the Bloch-like skyrmion texture, for the $[(SrTiO_3)_{16}/(PbTiO_3)_{16}]_8$ superlattice. Both are computed as in Ref.2, and are color coded with the key at right. Both b and c are overlaid by the polarization vectors. The arrows represent the components of the polarization in the *xy*-plane of the skyrmion. **d,** Macroscopic illustration of our $PbTiO_3$–$SrTiO_3$ system (details in method) (left) and it's corresponding circuit diagram (right). R_{ext} describes some external resistance of the circuit leading up to the thin film capacitor **e,** Given the values of the dielectric permittivity of $SrTiO_3$ (ε_1) to be 0-500 and inside/outside of the skyrmion within $PbTiO_3$ (ε_2) to be 0-500, an estimate of the value of the permittivity at the surface of the skyrmion (ε_3) is made to get the experimental value of the global effective dielectric constant ε_{eff}= 800, as measured experimentally in Fig. 1a. **f,** Taking the fixed dielectric permittivity of skyrmion wall as ε_3=1000, an estimation is made of the effective value as a function of ε_1 and ε_2. ε_{eff} is always positive and might be as large as ε_{eff} =8, which agrees with the classical result.

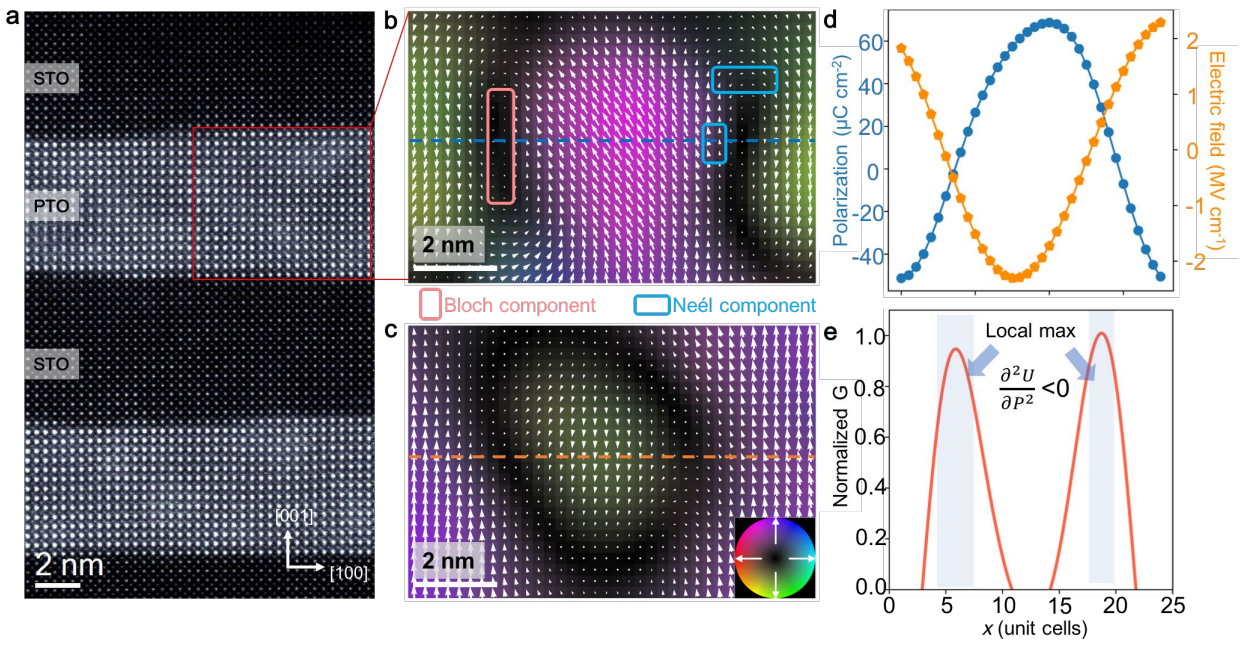

Figure 3| Measurement of local polarization, electric field, and local potential energy of the polar skyrmion using SCBED. a, A cross-sectional HAADF-STEM image of the skyrmions in $PbTiO_3$ layer, where we can access the cross-section of the Neél component and the Bloch component from the skyrmion wall. **b**, Polarization and **c,** electric field vector map of the skyrmion measured using SCBED for the cross-section geometry (*x*-*z* plane). **d**, Variation in the z components of local polarization (P_z; blue curve) and electric field (E_z; orange curve) along a horizontal line profile drawn through the center of a polar skyrmion, as indicated by dashed lines in b and c. **e**, Local potential energy estimated from the variation in P_z and E_z along the same line. Regions around the skyrmion walls (arrowed) do have a local energy higher than the surroundings with a negative curvature ($(\partial^2 U)/(\partial P^2) < 0$), indicating local negative permittivity.

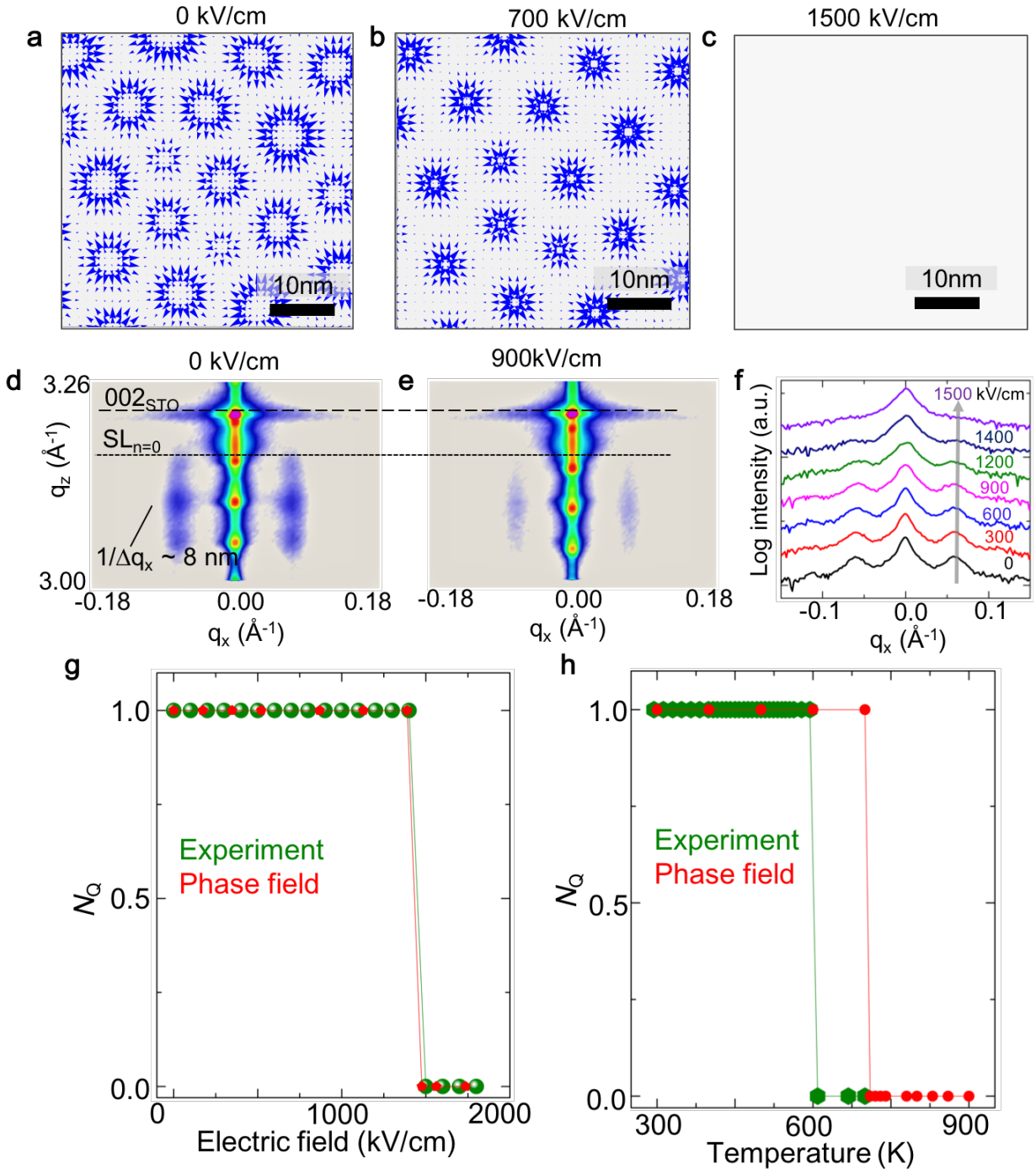

Figure 4| Electric field control of topological phase transition of polar skyrmion of $[(SrTiO_3)_{16}/(PbTiO_3)_{16}]_8$ superlattice. a-c, Phase field simulations show the shrinking of the diameters of the skyrmions under electric field (left to right), and ultimately the entire sample becomes uniformly ferroelectric ~ 1500 kV/cm. **d-e,** Electric field dependent reciprocal space maps shows the systematic disappearance of the satellite peaks (side-lobes, which correspond to

the skyrmions) with electric field. **f,** Intensity profile vs. electric field shows disappearance of the skyrmion peaks around ~1500 kV/cm (right). **g,** Dependence of topological number under the electric field. At ~ +1500 kV/cm topological number flip from +1 to zero indicating the topological skyrmion phase transfer to trivial single domain state. Topological number from a phase-field simulation (red symbols and lines) of the same $(SrTiO_3)_{16}/(PbTiO_3)_{16}$ superlattice, which closely match the experimental observations (green symbols and lines). **h,** Dependence of topological number under the temperature. Around ~600K topological number flip from +1 to zero indicating the topological skyrmion phase transfer to ferroelectric mono-domain state. This observation is slightly different from the phase field simulation due the strain relaxation (red symbols and line).

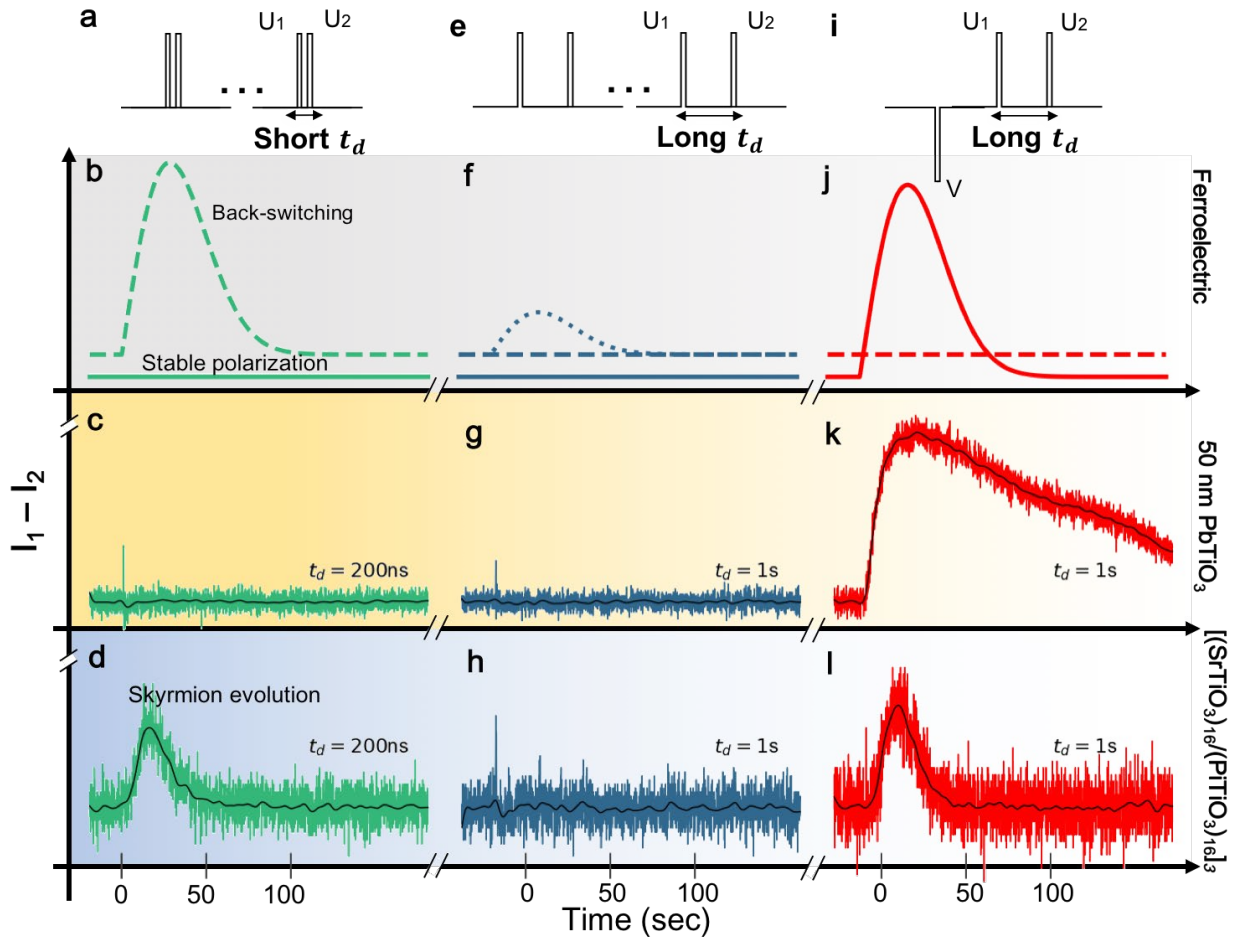

Figure 5| Generation of a Transient State with Time Dependent Capacitance. a, Schematic of two unipolar pulses (U_1 and U_2) applied to the sample with short delay time, t_d, between pulses. The initial pulse poles the sample to the uniform polarization state and initializes a transient state where the capacitance evolves in time. Zero field is applied in between pulses for time t_d, during which, the system begins to relax. We monitor the difference in current response to U_1 and U_2 ($I_1 - I_2$). **b,** shows the expected difference ($I_1 - I_2$) for a ferroelectric with (dashed green) and without back-switching (solid green). **c,** shows $I_1 - I_2$ for the parent ferroelectric (50 nm $PbTiO_3$ layer) as a flat difference, indicating a stable polarization. **d,** shows data for the superlattice with skyrmion with a notable peak, suggesting the existence of a relaxation process. To probe the timescale of relaxation we perform the experiment diagrammed in **e.**, changing to a long time delay, t_d. Expectation for a classical ferroelectric with complete back switching (long dash), partial back

switching (short dash) and stable ferroelectric polarization (solid) is shown in **f**. **g,** As expected, the parent 50nm $PbTiO_3$ layer shows a flat line, i.e., no difference. **h,** Notably, the superlattice also shows a flat difference indicating that relaxation has completed (t_d = 1s shown). Finally, we perform the experiment diagrammed in **i.** where we apply a preset pulse down pulse (V) and monitor $I_1 - I_2$ for long t_d. **j,** shows expectation from a ferroelectric, where a switchable, stable polarization (solid line) will result in a large $I_1 - I_2$ coming from the displacement current of a switching event, which only occurs in response to U_1 (I_1). A ferroelectric which undergoes complete back switching (dashed line) would show no difference $I_1 - I_2$ as in both cases the switching transient occurs. **k,** The parent 50 nm $PbTiO_3$ layer shows a large signal coming from the switchable remnant polarization. **l,** The $I_1 - I_2$ for the skyrmion sample, which importantly shows a distinguishable signal. This, in conjunction with the data in **d.** and **h.** indicates that the origin of the relaxation seen in the skyrmion sample is not back-switching of the small remnant polarization but rather a new, novel mechanism originating from the polar skyrmion structure.